Supporting Information

Synergistic Effects of Phosphorus Doping and Radial Pores in WSe_2/C Microspheres for Enhanced Room-Temperature NO_2 Sensing

Rui Ma[†#], Yuan Ren[†#*], Zi Ye[†], Jiayi Zhou[†], Yujia Chen[†], Qiongfeng Shi[‡], Li Tao[†*]

[†]School of Materials Science and Engineering, Jiangsu Key Laboratory for Advanced Metallic Materials, Southeast University, Nanjing 211189, P. R. China

[‡]School of Electronic Science and Engineering, Southeast University, Nanjing 211189, P. R. China

[#]These authors contribute equally to this work

*Email: renyuan@seu.edu.cn, tao@seu.edu.cn

Characterizations and measurements:

Field-emission scanning electron microscopy (FESEM) images were obtained with Crossbeam350 performed at 5 kV. Transmission electron microscopy (TEM) and high-resolution transmission electron microscopy (HRTEM) images were gained from Talos P200X G2 performed at 200 kV. X-Ray diffraction (XRD) patterns were collected with Ultima IV. X-ray photoelectron spectroscopy (XPS) data were tested on K-Alpha XPS System with MONO Al source (America). Thermogravimetric (TG) analysis data were obtained from 25 to 800 °C in air with a heating rate of 10 °C min^{-1} at PerkinElmer STA 8000 (America). N_2 adsorption-desorption isotherms were obtained at 77 K with Micromeritics ASAP 2460 (America). Before measurements, the samples were degassed in vacuum at 180 °C for 6 h to remove impurities. The specific surface area was recorded with Brunauer-Emmett-Teller (BET) method and the size distributions were dealt with Barrett-Joyner-Halenda (BJH) model. Raman spectroscopy data were collected form alpha300 Access.

Gas sensing performance evaluation:

25 mg of the powder material was mixed with 0.2 mL of anhydrous ethanol and ground mechanically in an agate mortar for 1 minute to form a homogeneous slurry. The resulting slurry was uniformly applied onto alumina ceramic tubes using a precision brush with the coating thickness controlled to 1–2 μm. After drying at ambient conditions (25 °C, 1 h), the coated tubes were thermally treated at 100 °C for 10 minutes in air to remove residual ethanol and activate surface sites before gas-sensing measurements. The distance between the two Au electrodes on alumina tubes was 2.0 mm on average. Then all the alumina tubes were fabricated into side-heated type of gas sensor and evaluated on SM1.1-G gas sensing measuring system with the 5 V bias voltage. The high concentration of gas is converted by volume and the corresponding concentration of gas is injected into the instrument chamber (1.8 L) using a syringe while other target liquid analytes were injected onto an evaporation plate to generate target gases. The test system reflects the gas sensing capability of the sensors by detecting changes in electrical resistance. The sensitivity is defined as $S = \Delta R/R_a$ (where

$\Delta R = R_a - R_g$, R_a and R_g is the resistance of the sensor in air and in target gas respectively). The response or recovery time was expressed as the time taken for the sensor output to reach 90 % of its saturation after applying or switching off the gas in a step function. The theoretical limit of detection (LOD) was determined according to the following formula according to the IUPAC definition of LOD, a true signal was when the signal-to-noise ratio is 3 or higher.

$$V_{x^2} = \sum (y_i - y)^2 \quad (1)$$

$$rms_{noisy} = \sqrt{\frac{V_{x^2}}{R_{average}}} \quad (2)$$

$$LOD\ (ppm) = 3\frac{rms_{noisy}}{slope} \quad (3)$$

(y_i, experimentally determined baseline data point; y, corresponding value of the fitting equation; $R_{average}$, average of baseline data; slope, linear regression fit of the sensor response vs NO_2 concentration plot; rms_{noise} represent the standard deviation of the baseline data).

Density functional theory calculations:

We have employed the Vienna Ab Initio Package (VASP)[1,2] to perform all spin-polarized density functional theory (DFT) calculations within the generalized gradient approximation (GGA) using the Perdew-Burke-Ernzerhof (PBE)[3] formulation. We have chosen the projected augmented wave (PAW) potentials[4,5] to describe the ionic cores and take valence electrons into account using a plane wave basis set with a kinetic energy cutoff of 450 eV. Partial occupancies of the Kohn−Sham orbitals were allowed using the Gaussian smearing method and a width of 0.05 eV. The electronic energy was considered self-consistent when the energy change was smaller than 10^{-5} eV. A geometry optimization was considered convergent when the energy change was smaller than 0.02 eV $Å^{-1}$. The vacuum spacing in a direction perpendicular to the plane of the structure is 18 Å. The weak interaction was described by DFT+D3 method using

empirical correction in Grimme's scheme[6, 7].

The adsorption energy (E_{ads}) was calculated using Eq. 4,

$$E_{ads}=E_{total}-E_{substrate}-E_{adsorbate} \quad (4)$$

The E_{total}, $E_{substrate}$ and $E_{adsorbate}$ represent the energy of adsorption structure, substrate and adsorbate (NO_2), respectively.

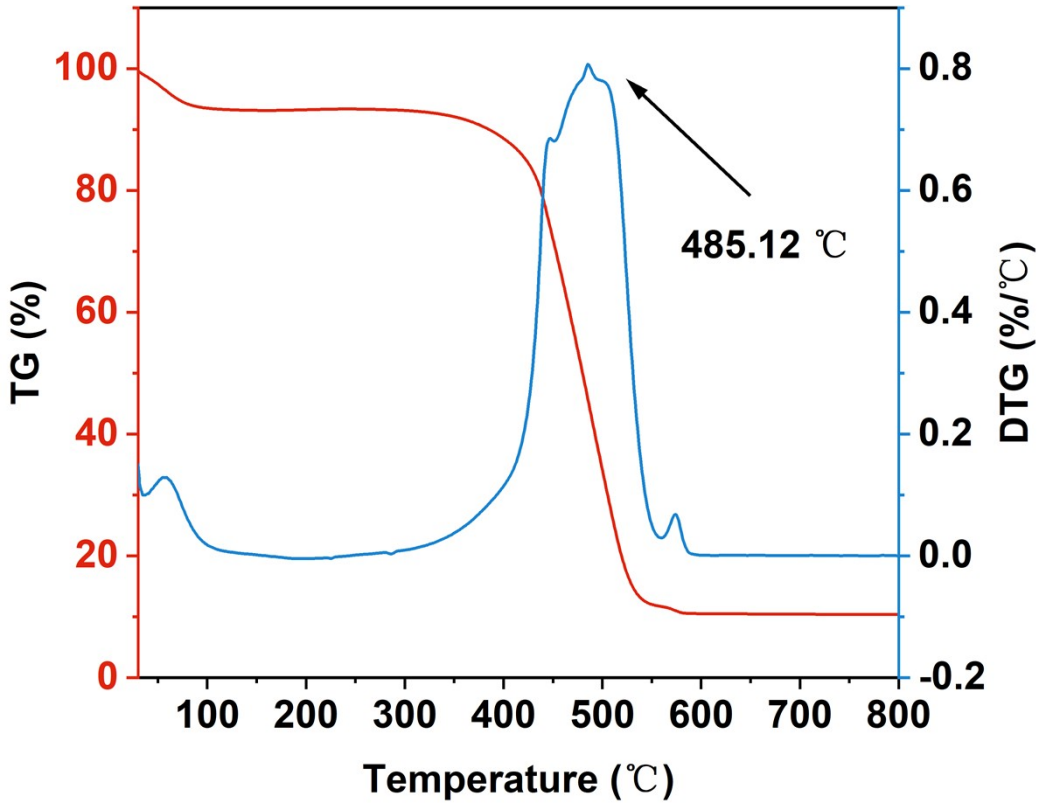

Figure S1. Thermogravimetric curve of mP-WSe_2/C in air.

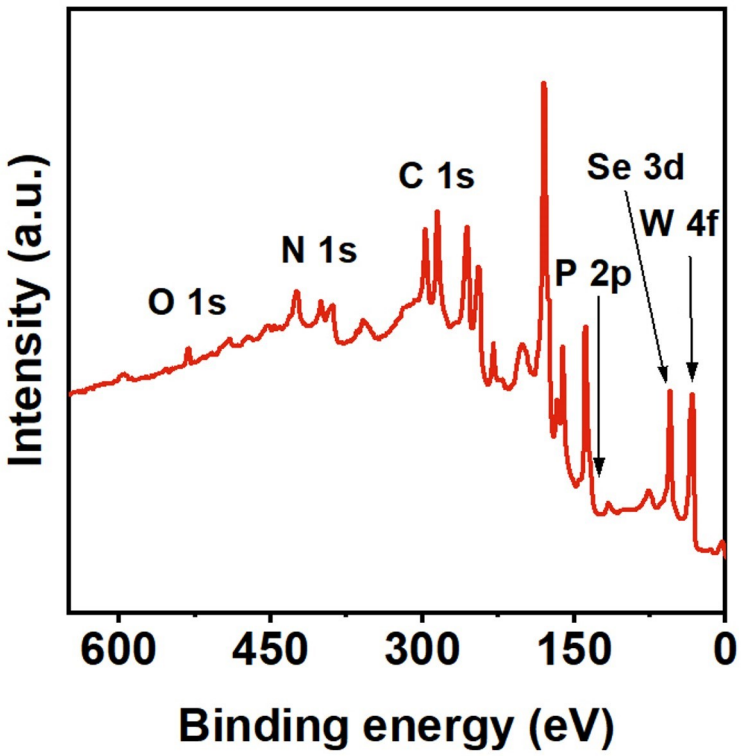

Figure S2. XPS spectrum of mP-WSe_2/C.

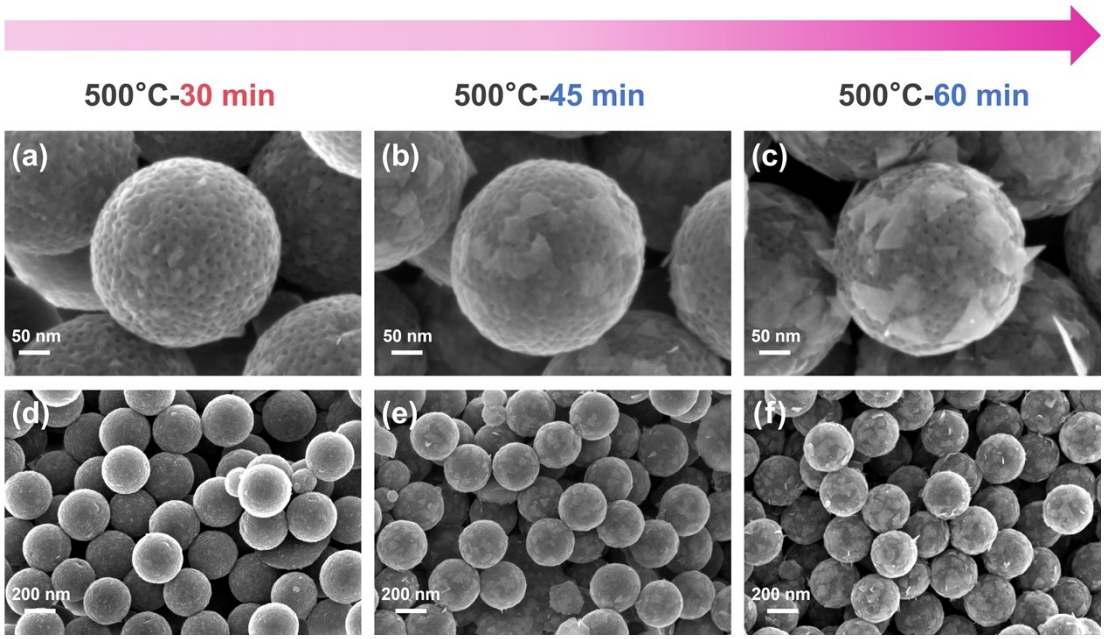

Figure S3. SEM images of the mP-WSe_2/C synthesized by different selenization times at 500 °C. (a, d) 30 min, (b, e) 45 min, (c, f) 60 min.

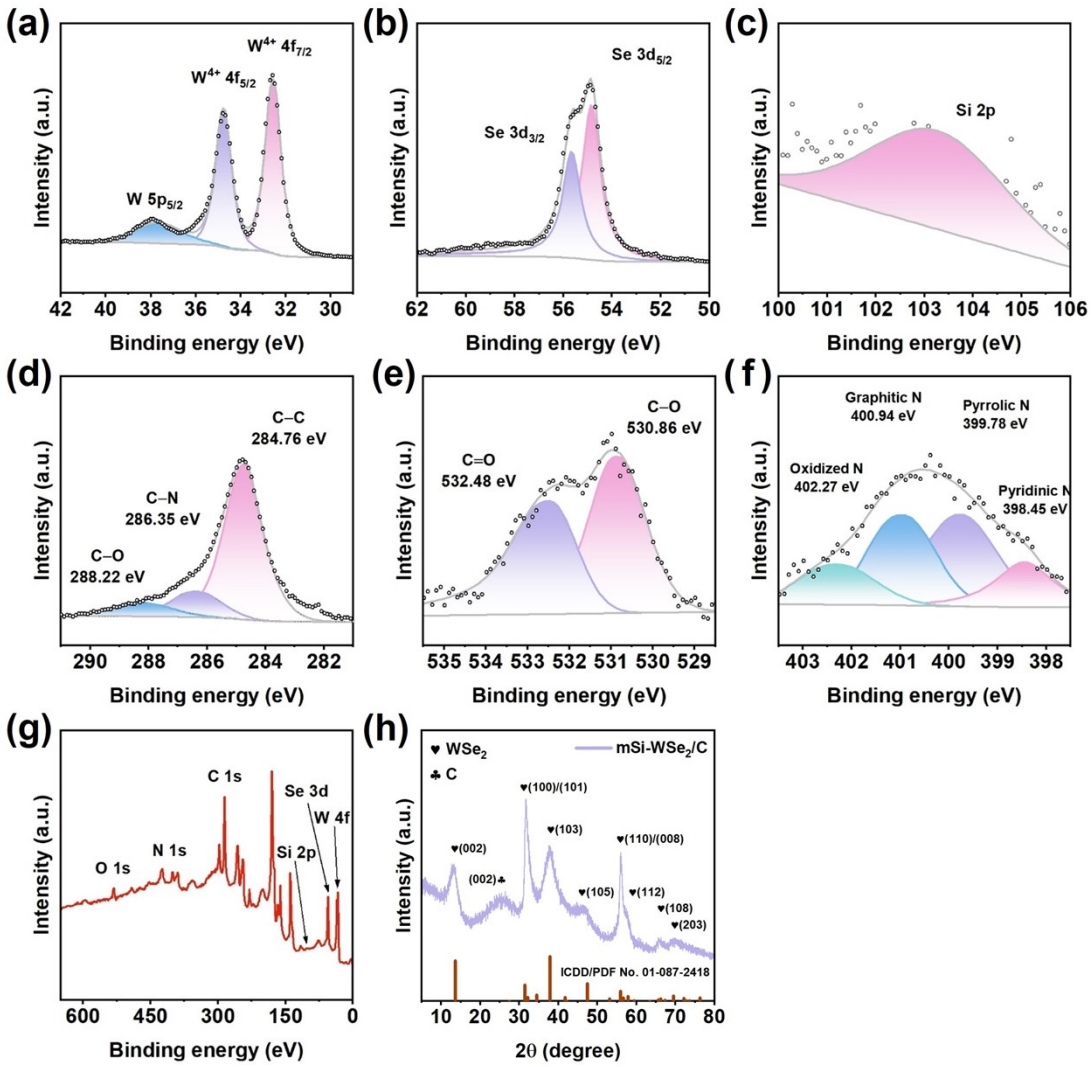

Figure S4. X-ray photoelectron spectroscopy of mSi-WSe_2/C. (a) W 4f, (b) Se 3d, (c) Si 2p, (d) C 1s, (e) O 1s, (f) N 1s core level peak regions and (g) the survey. (h) XRD pattern of P-mWSe_2-CM.

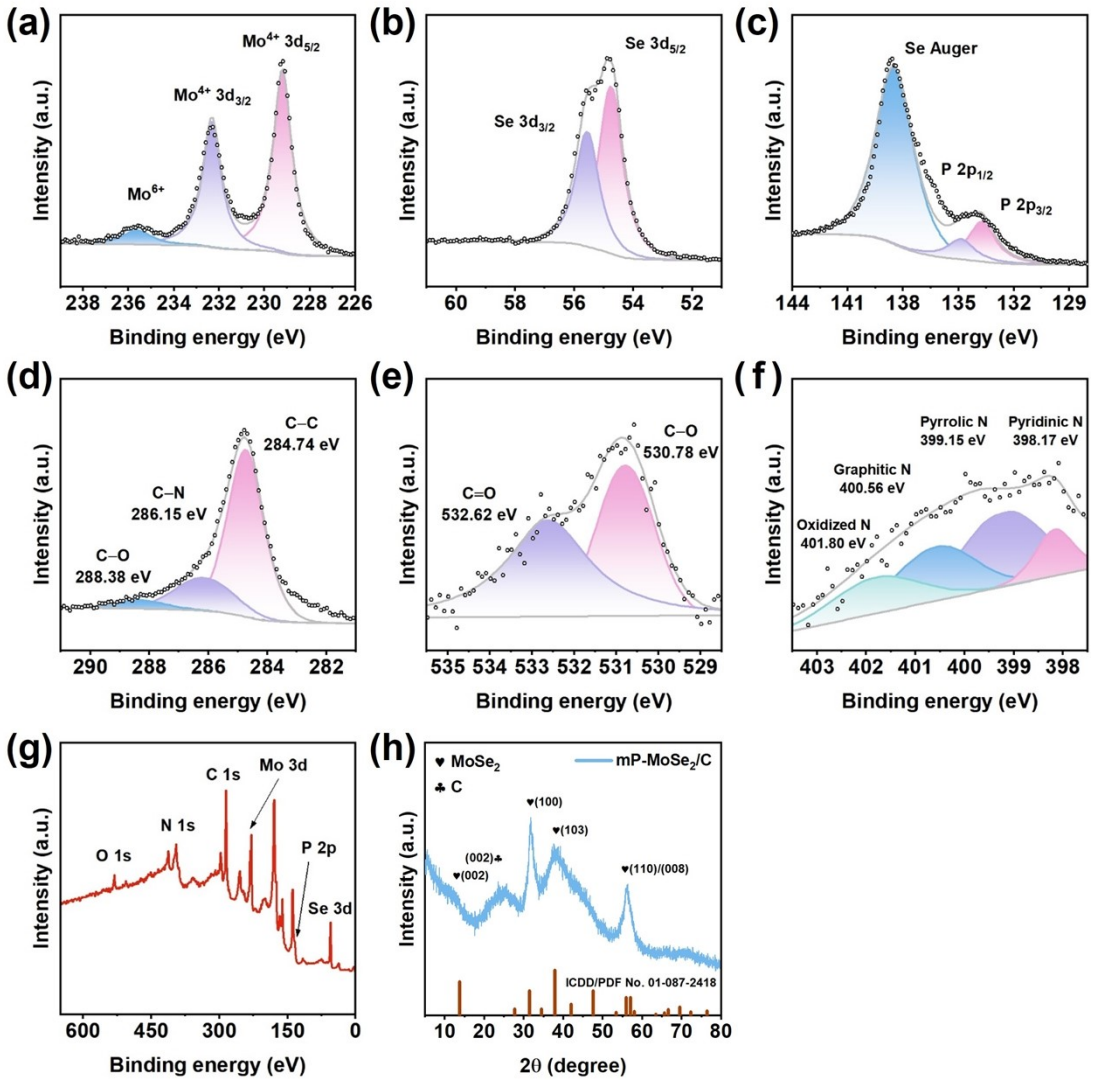

Figure S5. X-ray photoelectron spectroscopy of mP-$MoSe_2$/C. (a) Mo 3d, (b) Se 3d, (c) P 2p, (d) C 1s, (e) O 1s, (f) N 1s core level peak regions and (g) the survey. (h) XRD pattern of P-m$MoSe_2$-CM.

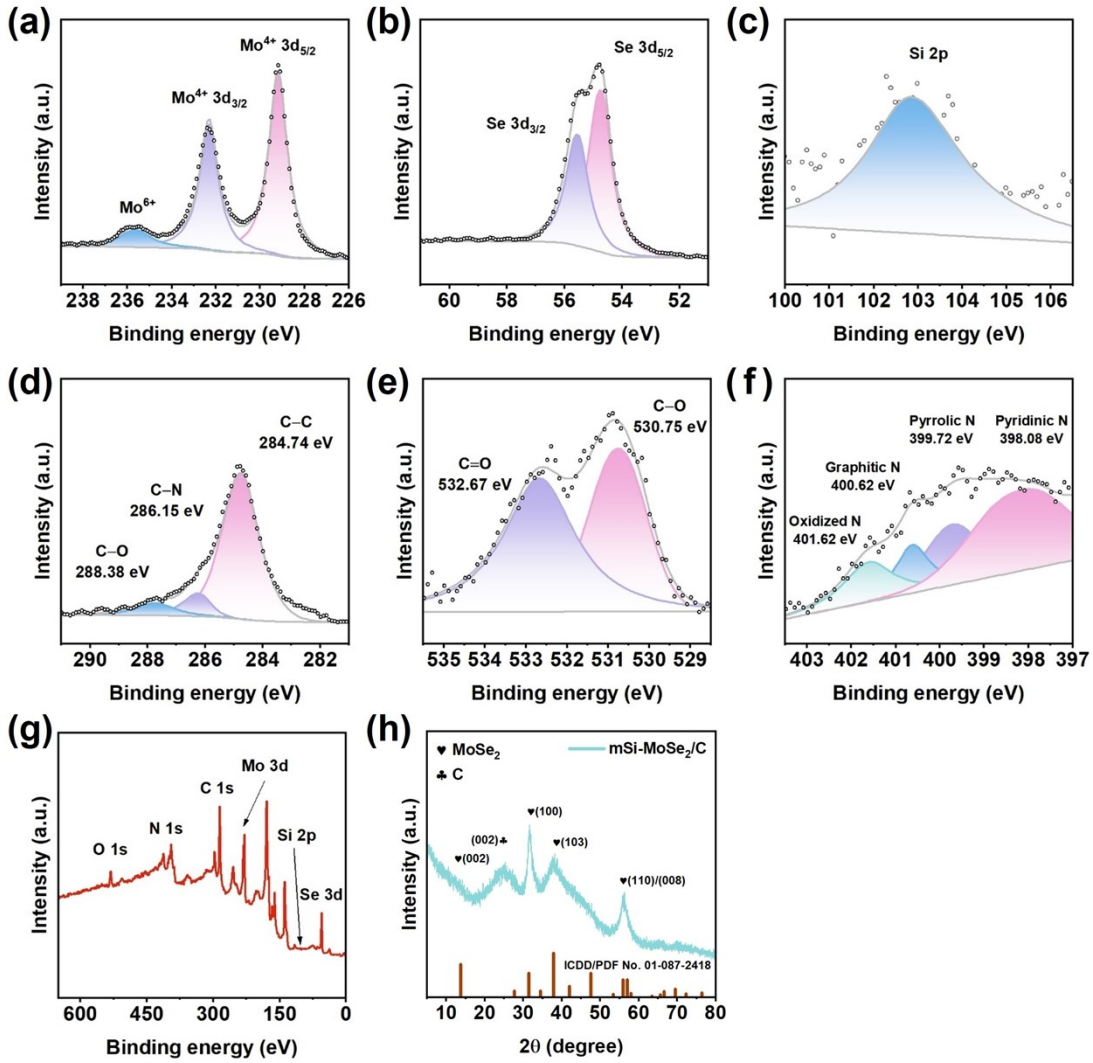

Figure S6. X-ray photoelectron spectroscopy of mSi-$MoSe_2$/C. (a) Mo 3d, (b) Se 3d, (c) Si 2p, (d) C 1s, (e) O 1s, (f) N 1s core level peak regions and (g) the survey. (h) XRD pattern of Si-m$MoSe_2$-CM.

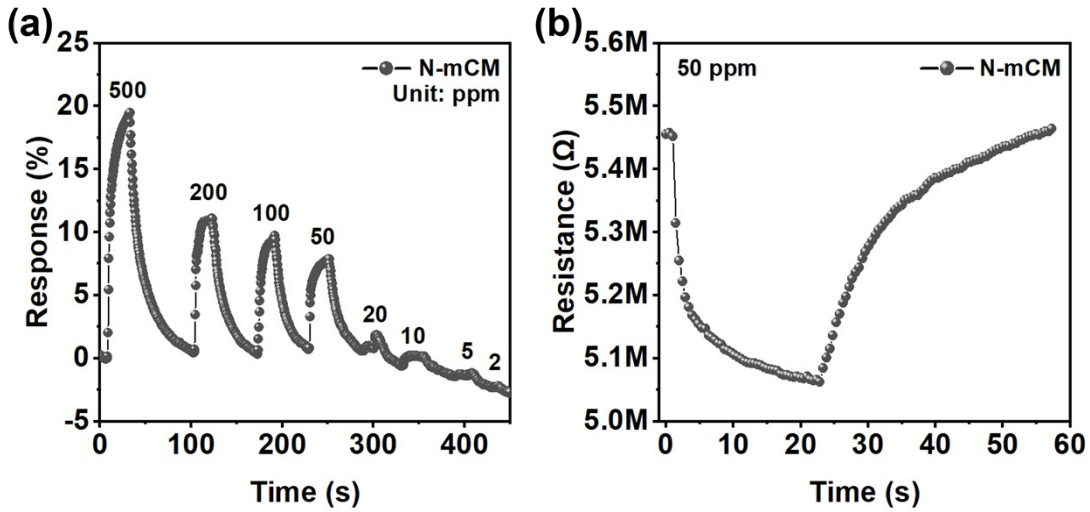

Figure S7. (a) Response and recovery curves of the N-mCM toward NO_2 of different concentrations (2-500 ppm) at room temperature. (b) Resistance change of N-mCM exposed to 50 ppm NO_2.

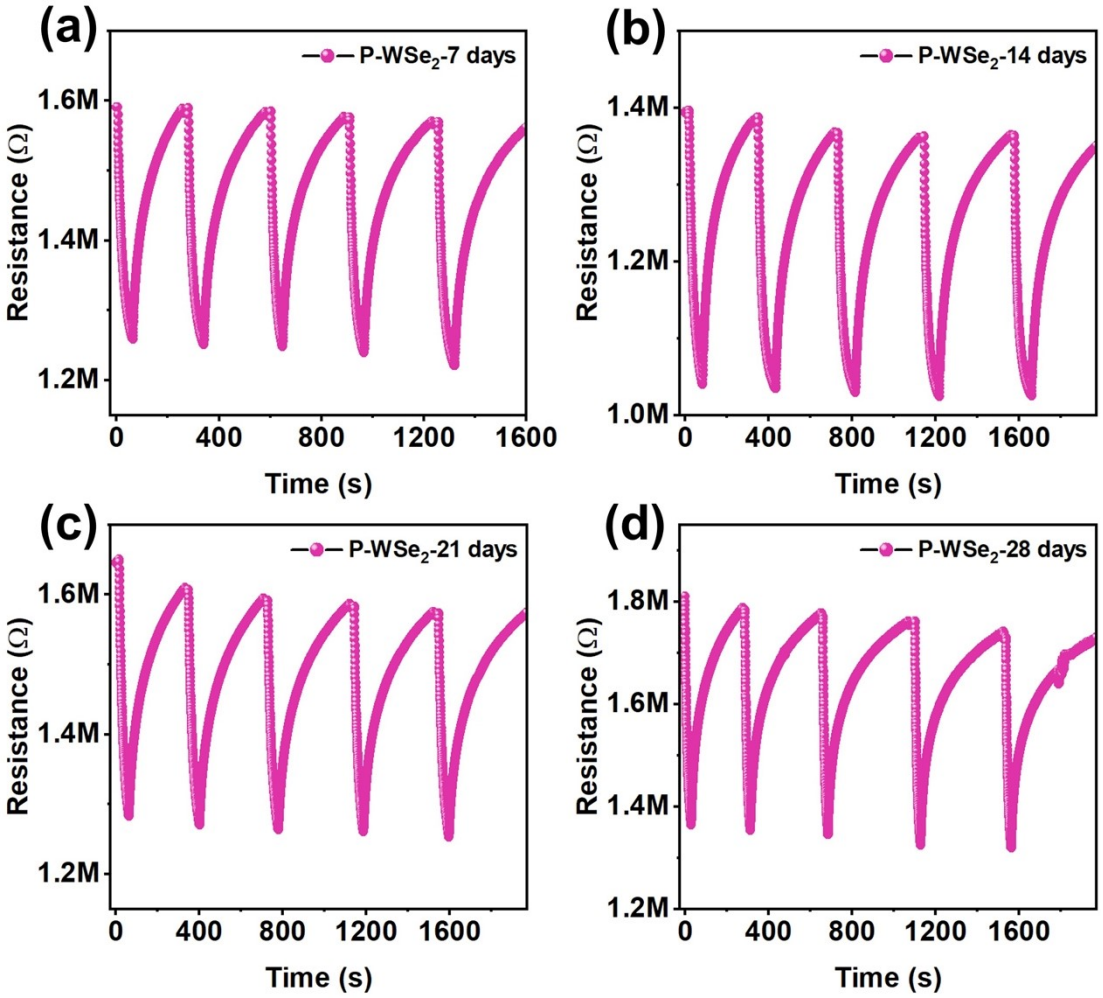

Figure S8. Cycling stability testing curves of mP-WSe_2/C at different times under 100 ppm NO_2 concentration.

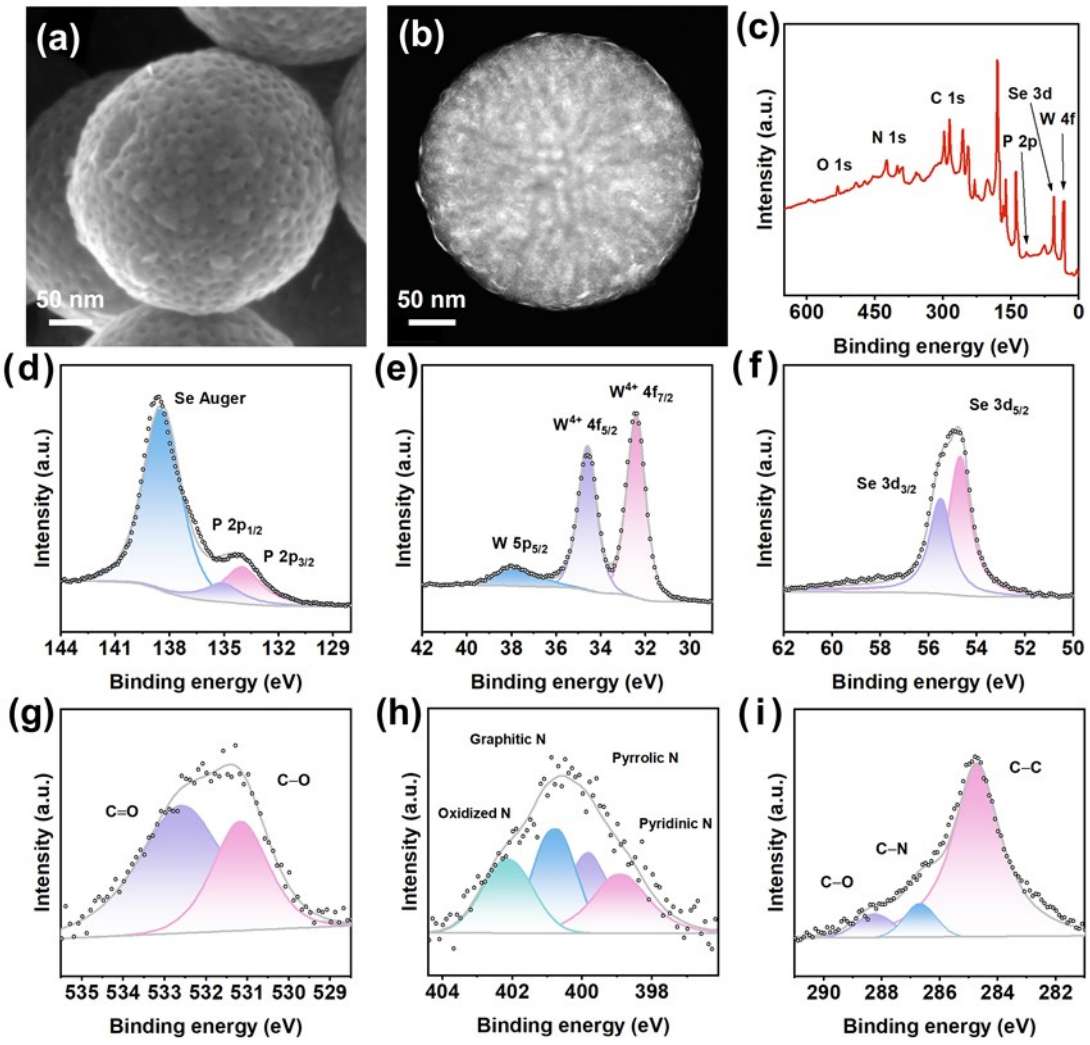

Figure S9. SEM (a) and TEM (b) image of P-mWSe$_2$/C after four weeks of operation are shown, along with XPS analyses including the survey spectrum (c) and core-level spectra of P 2p (d), W 4f (e), Se 3d (f), O 1s (g), N 1s (h), and C 1s (i).

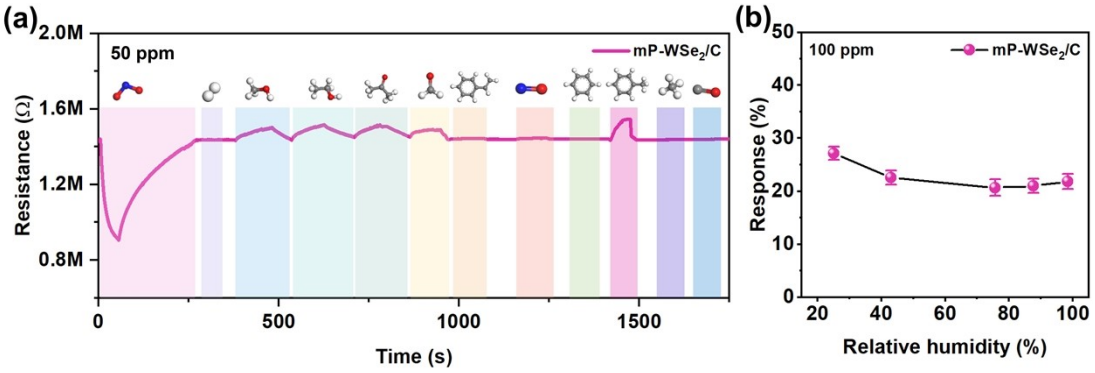

Figure S10. (a) Real-time dynamic response–recovery curves of the mP-WSe_2/C sensor to 12 gases. (b) Sensing response of the mP-WSe_2/C to 100 ppm NO_2 at different relative humidity.

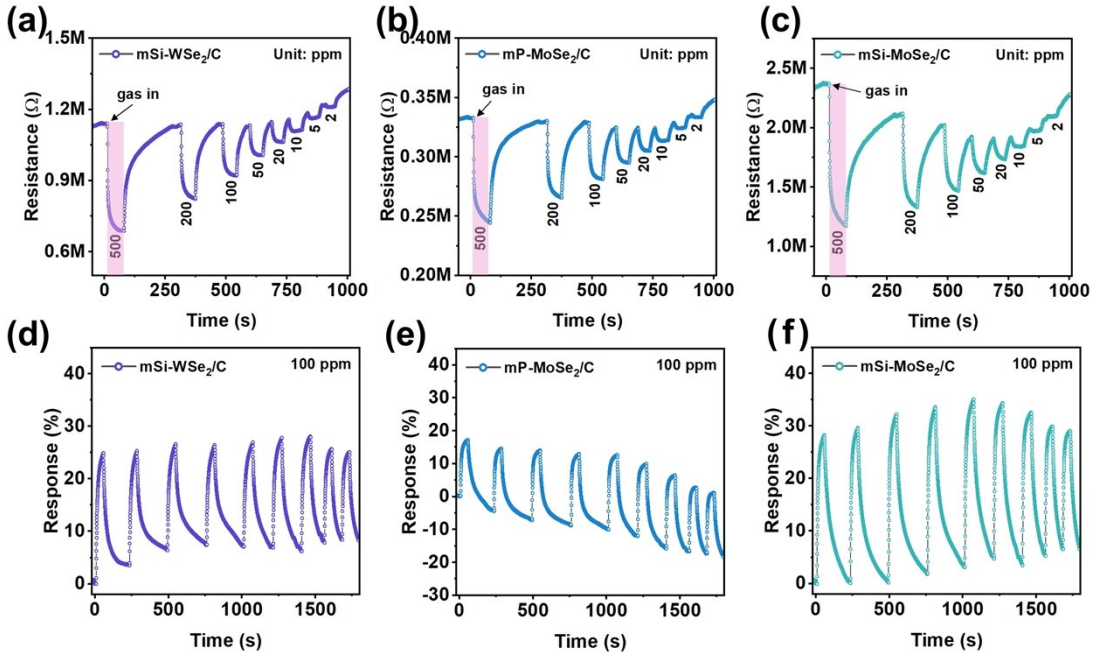

Figure S11. Response and recovery curves of the sensor towards NO_2 of different concentrations (2-500 ppm) and cycling stability testing curves towards 100 ppm NO_2 of (a, d) mSi-WSe_2/C, (b, e) mP-$MoSe_2$/C and (c, f) mSi-$MoSe_2$/C.

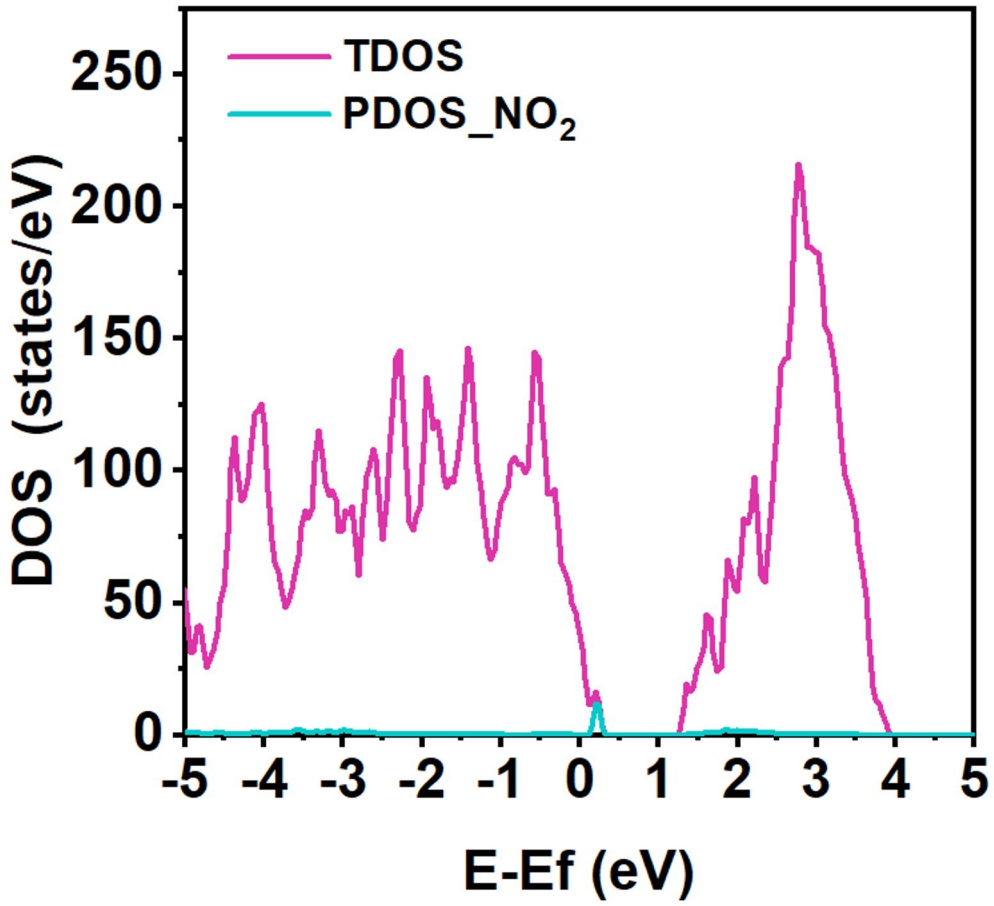

Figure S12. Total density of states (TDOS) of P-doped WSe_2 and partial density of states (PDOS) of NO_2.

Table S1. Comparison of sensitivity to NO_2 with analogous 2D material-based semiconductor gas sensors.

Materials	Operating Temperature	Concentration (ppm)	Response (%)	Response time (s)	Ref
MoS_2 film	RT	50	17.1	480	[8]
MoS_2/ GaN	RT	50	47.89	3600	[9]
SnS_2 flakes	RT	50	20	40	[10]
RuO_2/MoS_2	RT	50	21.39	81	[11]
SnO_2–graphene	RT	50	6	190	[12]
Bi_2Se_3 film	RT	5	120	81	[13]
MoS_2 NFs	RT	50	4	~25	[14]
WS_2	RT	50	15.7	166	[15]
MoS_2/MoO_3	RT	50			[16]
Cl-graphene	RT	5	2	38	[17]
MoS_2	RT	50	6	——	[18]
MoS_2/rGO	RT	50	16.9	~50	[19]
MoS_2/rGO/GQDs	RT	50	23	150	[19]
Porous WSe_2	RT	50	10	500	[20]
Au-MoS_2	RT	50	18	50	[21]
WSe_2	RT	500	100	390	[22]
$SnSe_2$	RT	100	22	——	[23]
MoS_2 /SnO_2	RT	10	28	408	[24]
MoS_2/WSe_2	RT	50	15	120	[25]
PbS/WSe_2	RT	50	15	30	[26]
MoS_2/CNT	RT	50	12.6	1200	[27]
rGO	RT	50	10.8	161	[28]
Ti_3C_2Tx	RT	50	11.9	40.4	[29]
mP-WSe_2/C	**RT**	**50**	**15**	**19**	**This**

REFERENCES

[1] Kresse, G.; Furthmüller, J. *Comput. Mater. Sci.* **1996**, 6, 15−50.

[2] Kresse, G.; Furthmüller, J. *Phys. Rev. B* **1996**, 54, 11169−11186.

[3] Perdew, J. P.; Burke, K.; Ernzerhof, M. *Phys. Rev. Lett.* **1996**, 77, 3865−3868.

[4] Kresse, G.; Joubert, D. *Phys. Rev. B* **1999**, 59, 1758-1775.

[5] Blöchl, P. E. *Phys. Rev. B* **1994**, 50, 17953-17979.

[6] Grimme, S.; Antony, J.; Ehrlich, S.; Krieg, S. *J. Chem. Phys.* **2010**, 132, 154104.

[7] Grimme, S.; Ehrlich, S.; Goerigk, L. *J. Comp. Chem.* **2011**, 32, 1456.

[8] Xu, T.; Pei, Y.; Liu, Y.; Wu, D.; Shi, Z.; Xu, J.; Tian, Y.; Li, X.; *J. Alloys Compd.* **2017**, 725, 253.

[9] Reddeppa, M.; Park, B.-G.; Murali, G.; Choi, S. H.; Chinh, N. D.; Kim, D.; Yang, W.; Kim, M.-D. *Sens. Actuators B: Chem.* **2020**, 308, 127700.

[10] Kumar, A.; Sharma, N.; Gutal, A. P.; Kumar, D.; Kumar, P.; Paranjothy, M.; Kumar, M.; *Sens. Actuators B: Chem.* **2022**, 353, 131078.

[11] Patil, S. V.; Kampara, R. K.; Venktesan, A.; Dongale, T. D.; Bae, J.; Devnath, A.; Seo, I.; Lee, S. *Alloys Compd.* **2025**, 1036, 181748.

[12] Liu, X.; Cui, J.; Sun J.; Zhang X. *RSC Adv.* **2014**,4, 22601-22605.

[13] Wang, Y.; Tang, C.; Su, M.; Ji, Y.; Xie, L.; Yang, Q.; Du, A.; Zhou, Y.; Yang, J. *Chin. Chem. Lett.* **2023**, 34, 107981.

[14] Luo, J.; Li, C.; Yang, Q.; Yan, L.; Zhang, B.; Tao, R. *IEEE Sens. J.* **2022**, 22, 7.

[15] Liang, Z.; Zhang, X.; Yang, J.; Cheng, Y.; Hou, H.; Hussain, S.; Liu, J.; Qiao, G.; Liu, G. *J. Hazard. Mater.* **2023**, 443, 130316.

[16] Ko K. Y.; Song, J.-G.; Kim, Y.; Choi, T.; Shin S.; Lee, C. W.; Lee, K.; Koo, J.; Lee, H.; Kim, J.; Lee T.; Park, J.; Kim, H. *ACS Nano* **2016**, 10, 9287–9296

[17] Oh, J.; Kim, H.; Cho, S.; Sim, J.; Choi, S; Kim, A.; Lee, W.; An, S.; Hong, B. H.; Lee, D.; Kim, Y. *J. Mater. Chem. A* **2025**,13, 39704-39713.

[18] Cho, S.-Y.; Kim, S. J.; Lee, Y.; Kim, J.-S.; Jung W.-B.; Yoo, H.-W.; Kim, J.; Jung, H.-T. *ACS Nano* **2015**, 9, 9314–9321.

[19] Yang, C.; Wang, Y.; Wu, Z.; Zhang, Z.; Hu, N.; Peng, C. *Nanomaterials* **2022**, 12, 901.

[20] Kang, M. J.; Kim, J.; Seo, J.; Lee, S.; Park, C.; Song, S.; Kim, S.S.; Hahm, M.G. *Phys. Status Solidi RRL*, **2019**, 13, 1900340.

[21] Hu, J.; Liu, X.; Zhang, J.; Gu, X.; Zhang, Y.; *Sensor. Actua, B: Chem.* **2023**, 382, 133505.

[22] Ko, K.; Park, Y. K.; Lee, S.; Kim, Y.; Woo, W. J.; Kim, D.; Song, J.-G.; Park, J.; Kim, H. *ACS Appl. Mater. Interfaces* **2018**, 10, 23910−23917.

[23] Hwa, Y.; Seok, B.; Chee, SS.; *Electron. Mater. Lett.* **2023**,19, 212–217.

[24] Cui, S.; Wen, Z.; Huang, X.; Chang, J.; Chen, J. *Small* **2015**, 11, 2305-2313.

[25] Kim, Y.; Lee, S.; Song, J.-G.; Ko, K. Y.; Woo, W. J.; Lee, S. W.; Park, M.; Lee, H.; Lee, Z.; Choi, H.; Kim, W.-H.; Park, J.; Kim, H.; *Adv. Funct. Mater.* **2020**, 30, 2003360.

[26] Xin, X.; Zhang, Y.; Guan, X.; Cao, J.; Li, W.; Long, X.; Tan, X. *ACS Appl. Mater. Interfaces* **2019**, 11, 9438−9447.

[27] Deokar, G.; Vancsó, P.; Arenal, R.; Ravaux, F.; Casanova-Cháfer, J.; Llobet, E.; Makarova, A.; Vyalikh, D.; Struzzi, C.; Lambin, P.; Jouiad, M.; Colomer, J. *Adv. Mater. Interfaces.* **2017**, 4, 1700801.

[28] Kumar, N.; Srivastava, A. K.; Patel, H. S.; Gupta, B. K.; Varma, G. D. *Eur. J. Inorg. Chem.* **2015**, 2015, 1912.

[29] Guo, F.; Feng, C.; Zhang, Z.; Zhang, L.; Xu, C.; Zhang, C.; Lin, S.; Wu, H.; Zhang, B.; Tabusi, A.; Huang, Y. *Sensor. Actua, B: Chem*. **2023**, 375, 132885